Dynamic Modeling and Sensitivity Analysis of Stiffness Modulations Induced by Pitting Evolution in Spur Gear

Yakeu Happi Kemajou Herbert * and Tchomeni Kouejou Bernard Xavier

Posted Date: 4 May 2026

doi: 10.20944/preprints202605.0061.v1

Keywords: spur gearbox; pitting fault; mesh stiffness; vibration analysis; fault diagnosis; condition monitoring; torsional–lateral dynamics; sensitivity analysis

 doi:10.20944/preprints202605.0061.v1

Article

Dynamic Modeling and Sensitivity Analysis of Stiffness Modulations Induced by Pitting Evolution in Spur Gear

Yakeu Happi Kemajou Herbert * and Tchomeni Kouejou Bernard Xavier

Vaal University of Technology, Department of Industrial Engineering, Operation Management and Mechanical Engineering, Vanderbijlpark, South Africa

* Correspondence: kemajouy@vut.ac.za

Abstract

In this study, a six-degree dynamic model considering torsion and bending is proposed for a single-stage spur gear reducer. The objective is to study the effect of progressive pitting on the dynamic behavior of the system. The evolution of mesh stiffness over time is modeled using an energy-based approach that takes into account the geometric characteristics of pitting defects, including their depth, width, and location on the gear teeth. The equations of motion are obtained using the Lagrangian method and subsequently solved numerically using the Runge-Kutta scheme. Vibration responses are analyzed in the time, frequency, and time-frequency domains for both healthy and damaged gears. The results show that the onset of pitting leads to a significant loss of stiffness, amplitude modulation, and the appearance of spectral sidebands near the mesh frequency. A quantitative parametric sensitivity analysis reveals that the apparent contact velocity plays a predominant role at low speeds and in the early stages of damage. In contrast, at high speeds and advanced degradation levels, pit depth and width become dominant. The proposed methodology provides valuable comprehension into the propagation mechanisms of pitting faults and offers practical guidance for early failure detection and condition-based maintenance of gear drive system.

Keywords: spur gearbox; pitting fault; mesh stiffness; vibration analysis; fault diagnosis; condition monitoring; torsional–lateral dynamics; sensitivity analysis

1. Introduction

Gear drive systems are widely used in industrial machinery, automotive transmissions, and power conversion equipment due to their high efficiency and compact size. Their reliability is critical, as a failure can lead to unexpected production downtime, increased maintenance costs, and safety hazards.

Among the damage mechanisms affecting spur gears, tooth pitting is one of the most prevalent forms of surface fatigue. This phenomenon, initiated by Hertzian contact stresses at the mesh interface, causes progressive removal of material from the tooth flank. Its development alters the contact geometry and load distribution, leading to reduced stiffness, increased vibration and noise levels, and, in severe cases, can cause secondary failures such as chipping and tooth breakage.

In recent years, considerable research efforts have been devoted to understanding the dynamic behavior of gear systems exhibiting surface faults. Junguo et al. [1] continued the analysis by considering the flexion-torsion coupling, showing that these multidirectional interactions amplify the vibration characteristics associated with faults, which a purely torsional model can not accurately capture. This work emphasises the need for models with multiple degrees of freedom to faithfully represent the dynamics of damaged gears.

Recent advances also focus on intelligent diagnostics and physics-informed modeling. Zhang [2] proposed a dual-channel fuzzy convolutional neural network for gearbox diagnosis, achieving high

 doi:10.20944/preprints202605.0061.v1

accuracy. Zeng et al. [3] highlighted how stiffness variations induced by a fault significantly modulate the vibration response, particularly in the frequency domain. However, these data-driven approaches often provide limited physical interpretation of the degradation mechanisms.

Meanwhile, He et al. [4] studied the influence of thermo-elastohydrodynamic lubrication on the dynamics, revealing that thermal and tribological effects also modify mesh stiffness and dynamic response, particularly under severe conditions.

From a modeling perspective, Luo et al. [5] developed a dynamic model to describe tooth gap and spalling, which was experimentally validated. Their work shows that surface defects introduce nonlinear excitations and amplitude modulation in the vibration signals. Liang et al. [6] calculated the relationship between defect progression and vibration evolution. These studies build on the pioneering analytical frameworks established by El Badaoui et al. [7] to model localised faults and their detectability by vibration analysis.

To improve fault detection in non-stationary conditions, time-frequency analysis techniques are widely adopted. The wavelet transform, applied to diagnosis by Peng and Chu [8], proved effective in identifying the transient signatures of localised faults. Similarly, Fu et al. [9] demonstrated that advanced dynamic modeling coupled with frequency analysis effectively distinguishes between healthy and degraded states in multistage transmissions.

Although significant progress has been made in numerical modeling and signal processing, few comprehensive analytical frameworks exist that can explicitly link, based on fundamental principles of mechanics, the geometric parameters of faults to coupled torsional and bending dynamics. In particular, the quantitative influence of fault geometry on intrinsic gear parameters such as the contact ratio has not yet been systematically evaluated as a function of rotational speed using a unified approach based on sensitivity analysis.

A coupled dynamic model in torsion and bending with six degrees of freedom was developed using the Lagrange formalism. This approach allows for the simultaneous representation of shaft torsion, gear rotation, and lateral displacements, thus providing a more accurate description of the physical behavior than purely torsional models. Unlike conventional formulations that rely on empirical correction factors to simulate stiffness loss, the proposed model analytically derives the degradation of mesh stiffness from potential energy principles. Each pit is explicitly described by three geometric parameters: its depth, radius, and angular position. This representation allows for the precise capture of stiffness asymmetries and local modulation effects throughout the meshing cycle. A systematic parametric sensitivity analysis was then performed to evaluate, for different rotational speeds, the relative influence of the gear ratio and the depth, width, and angular position parameters of the fault. The results highlight a clear transition in the dominant parameters as a function of rotational speed: at low speeds, the dynamic behavior is primarily governed by the gear ratio; at higher speeds and in the presence of advanced pitting, the geometric parameters of the defect depth and width become the main contributors to vibration amplification.

This integrated approach, combining physical modeling and sensitivity analysis, provides a robust methodological basis for interpreting the vibration signatures associated with the evolution of surface defects and for guiding the development of predictive maintenance strategies adapted to different operating regimes.

The remainder of this article is organized as follows: Section 2 describes the mechanical configuration of the spur gear system and its degrees of freedom. Section 3 establishes the equations of motion and presents the formulation of the time-varying mesh stiffness, incorporating the geometry of fatigue pits. Section 4 presents the results of the dynamic analyses and the parametric sensitivity study. Section 5 discusses the mechanical implications related to stiffness modulation and the evolution of defects. Finally, a conclusion summarises the main contributions of this study and suggests approaches for future research.

 doi:10.20944/preprints202605.0061.v1

2. Study of One-Stage Spur Gear System

In this study, the assembly uses two gears, which allow a precise alignment of the shaft to form a dynamic drive system, all supported by four bearings. As illustrated in Figure 1 , the dynamic model of a single tooth pair is frequently used in the literature to describe the dynamic behavior of gears as a function of the operating cycle. The torque applied to the drive gear is denoted T_m and that to the driven gear, T_L. The total damping coefficient of the system is symbolized by c_t (in N·s/m) and the stiffness of the mesh by k_t (in N/m). For this model, six degrees of freedom are considered: the lateral displacements y_1 (pinion) and y_2 (wheel), the rotations θ_1 (pinion) and θ_2 (wheel), as well as the angular displacement θ_m(motor initial) and θ_L(load initial). It should be noted that for a spur gear, lateral vibrations in the x direction are not connected to those in the *y* direction, thus justifying the chosen configuration.

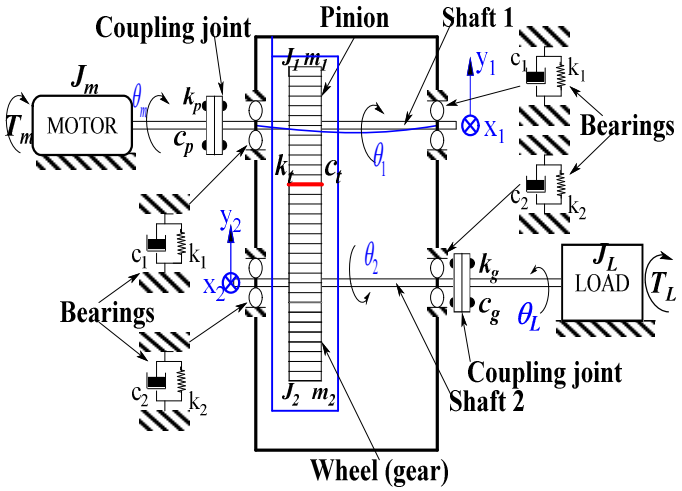

Figure 1. Kinematic diagram of a single-stage gearbox (6 DOF).

To create a model system, Lagrange dynamics in the inertial coordinates are used. The following section provides more specific information regarding the consideration of adjustment pitting fault in the one-stage spur gear system.

3. Governing Equations of Dynamic Model

This section details the mathematical formulation of the proposed dynamic model. The drive system is modeled by considering the torsional and lateral movements of the gear pair. The equations of motion are established using the Lagrange formalism.

The total kinetic energy of the system, denoted T, is derived from the geometry of Figure 1:

$$T=\frac{1}{2}m_1\dot{x}_1^2+\frac{1}{2}m_2\dot{x}_2^2+\frac{1}{2}m_1\dot{y}_1^2+\frac{1}{2}m_2\dot{y}_2^2+\frac{1}{2}J_1\dot{\theta}_1^2+\frac{1}{2}J_2\dot{\theta}_2^2+\frac{1}{2}J_m\dot{\theta}_m^2+\frac{1}{2}J_L\dot{\theta}_L^2 \quad (1)$$

where, m_1 , m_2 are gear mass; J_1 , J_2 are mass moment of initial of pinion and wheel; J_m , J_{load} are mass moment of initial of motor and load.

The total potential energy U of the gear system includes the strain energy of the rotating wheels. It is expressed as:

$$U=\frac{1}{2}k_1\left(x_1^2+y_1^2\right)+\frac{1}{2}k_2\left(x_2^2+y_2^2\right)+\frac{1}{2}k_p\left(\theta_m-\theta_1\right)^2+\frac{1}{2}k_g\left(\theta_2-\theta_L\right)^2+\frac{1}{2}k_t\left[\left(y_1+R_1\theta_1\right)-\left(y_2+R_2\theta_2\right)\right]^2 \quad (2)$$

where, k_1, k_2 are bearing stiffness; k_p, k_g are input torsional and output torsional stiffness; R_1 , R_2 are radius of pinion and wheel.

Finally, the Rayleigh dissipation function D, which takes into account viscous damping in the system, is given by:

 doi:10.20944/preprints202605.0061.v1

$$D=\frac{1}{2}c_1\left(\dot{x}_1^2+\dot{y}_1^2\right)+\frac{1}{2}c_2\left(\dot{x}_2^2+\dot{y}_2^2\right)+\frac{1}{2}c_p\left(\dot{\theta}_m-\dot{\theta}_1\right)^2+\frac{1}{2}c_g\left(\dot{\theta}_2-\dot{\theta}_L\right)^2+\frac{1}{2}c_t\left[\left(\dot{y}_1+R_1\dot{\theta}_1\right)-\left(\dot{y}_2+R_2\dot{\theta}_2\right)\right]^2 \quad (3)$$

where subscript 1 designates the drive gear and subscript 2, the driven gear.

After differentiating and rearranging the terms, and substituting the expressions for kinetic and potential energy in the Lagrange equation, the equations of motion with six degrees of freedom for the spur gear pair are obtained:

$$m_1\ddot{y}_1+c_1\dot{y}_1+c_t\left[\left(\dot{y}_1+R_1\dot{\theta}_1\right)-\left(\dot{y}_2+R_2\dot{\theta}_2\right)\right]+k_1y_1+k_t\left[\left(y_1+R_1\theta_1\right)-\left(y_2+R_2\theta_2\right)\right]=0 \quad (4)$$

$$m_2\ddot{y}_2+c_2\dot{y}_2-c_t\left[\left(\dot{y}_1+R_1\dot{\theta}_1\right)-\left(\dot{y}_2+R_2\dot{\theta}_2\right)\right]+k_2y_2-k_t\left[\left(y_1+R_1\theta_1\right)-\left(y_2+R_2\theta_2\right)\right]=0 \quad (5)$$

$$\begin{aligned}&J_1\ddot{\theta}_1-c_p\left(\dot{\theta}_m-\dot{\theta}_1\right)+k_t\left(R_1y_1+R_1^2\theta_1-R_1y_2-R_1R_2\theta_2\right)-k_p\left(\theta_m-\theta_1\right)+\\&c_t\left(R_1\dot{y}_1+R_1^2\dot{\theta}_1-R_1\dot{y}_2-R_1R_2\dot{\theta}_2\right)=0\end{aligned} \quad (6)$$

$$\begin{aligned}&J_2\ddot{\theta}_2+k_g\left(\theta_2-\theta_b\right)-k_t\left(R_2y_1+R_1R_2\theta_1-R_2y_2-R_2^2\theta_2\right)+c_g\left(\dot{\theta}_2-\dot{\theta}_L\right)+\\&c_t\left(R_2\dot{y}_1+R_1R_2\dot{\theta}_1-R_2\dot{y}_2-R_2^2\dot{\theta}_2\right)=0\end{aligned} \quad (7)$$

$$J_m\ddot{\theta}_m+k_p\left(\theta_m-\theta_1\right)+c_p\left(\dot{\theta}_m-\dot{\theta}_1\right)=T_m \quad (8)$$

$$J_L\ddot{\theta}_L+k_g\left(\theta_4-\theta_L\right)+c_g\left(\dot{\theta}_4-\dot{\theta}_L\right)=-T_L \quad (9)$$

The equations of motion governing the gear system are establishing in the matrix form as follows,

$$\begin{bmatrix} m_{y_1} & 0 & 0 & 0 & 0 & 0\\ 0 & m_{y_2} & 0 & 0 & 0 & 0\\ 0 & 0 & m_{\theta_1} & 0 & 0 & 0\\ 0 & 0 & 0 & m_{\theta_2} & 0 & 0\\ 0 & 0 & 0 & 0 & m_{\theta_m} & 0\\ 0 & 0 & 0 & 0 & 0 & m_{\theta_L} \end{bmatrix}\begin{Bmatrix}\ddot{y}_1\\ \ddot{y}_2\\ \ddot{\theta}_1\\ \ddot{\theta}_2\\ \ddot{\theta}_m\\ \ddot{\theta}_L\end{Bmatrix}+\begin{bmatrix} c_1+c_t & -c_t & R_1c_t & -R_2c_t & 0 & 0\\ -c_t & c_2+c_t & -R_1c_t & R_2c_t & 0 & 0\\ R_1c_t & -R_1c_t & R_1^2c_t+c_p & -R_1R_2c_t & -c_p & 0\\ -R_2c & R_2c_t & -R_1R_2c_t & \frac{2}{2}c_t+c_g & 0 & -c_g\\ 0 & 0 & -c_p & 0 & -c_p & 0\\ 0 & 0 & 0 & -c_g & 0 & 0 \end{bmatrix}\begin{Bmatrix}\dot{y}_1\\ \dot{y}_2\\ \dot{\theta}_1\\ \dot{\theta}_2\\ \dot{\theta}_m\\ \dot{\theta}_L\end{Bmatrix}$$

$$+\begin{bmatrix} k_1+k_t & -k_t & R_1k_t & -R_2k_t & 0 & 0\\ -k_t & k_2+k_t & -R_1k_t & R_2k_t & 0 & 0\\ R_1k_t & -R_1k_t & R_1^2k_t+k_p & -R_1R_2k_t & -k_p & 0\\ -R_2k_t & R_2k_t & -R_1R_2c_t & R_2^2k_t+k_g & 0 & -k_g\\ 0 & 0 & -k_p & 0 & -k_p & 0\\ 0 & 0 & 0 & -k_g & 0 & k_g \end{bmatrix}\begin{Bmatrix}y_1\\ y_2\\ \theta_1\\ \theta_2\\ \theta_m\\ \theta_L\end{Bmatrix}$$

This method provides a systematic framework for integrating the effects of kinetic energy, potential energy, and dissipation.

Excitations due to time-varying mesh stiffness and transmission error are explicitly included in the model to reflect the influence of pitting faults on the dynamic response.

3.1. Dynamic Distribution of Pitting on Tooth

The uniform distribution of pitting along the tooth width direction is shown in Figure 2.

 doi:10.20944/preprints202605.0061.v1

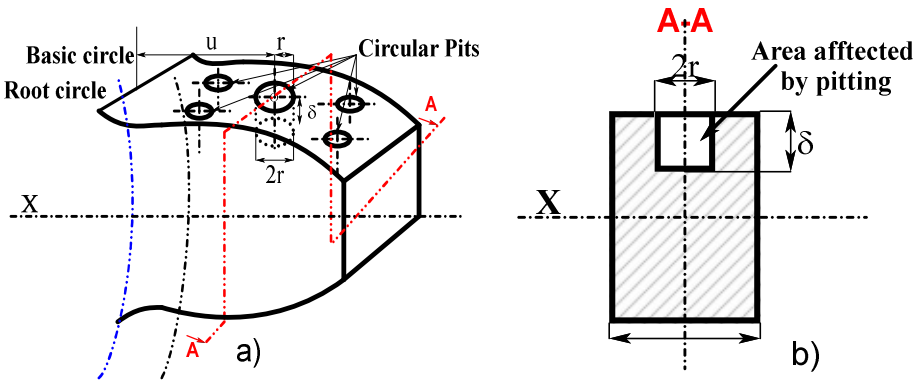

Figure 2. Gear tooth with holes: a) 3D perspective view of the profile and b) Cross section of the tooth.

3.2. Derivation of Gear Mesh Stiffness with Pitted Tooth

The influence of a pitted tooth on the stiffness of the mesh is evaluated using an energy-based approach using potential energy. As illustrated in Figure 2, a pinion tooth is modeled as a non-uniform cantilever beam from to the root circle.

When the tooth surface is affected by pitting distributed over several adjacent teeth, the effective contact length L is no longer constant; it decreases during meshing. This change affects the expressions for the contact length, cross-sectional area, and second moment of area, which then differ from those of a perfect tooth.

To calculate this reduction, the coefficients $\Delta_{L(x)}$, $\Delta_{A(x)}$, and $\Delta_{I(x)}$ are introduced, representing the reduction in the contact length (L_x), cross-sectional area (A_x), and moment of inertia of the tooth (I_x), respectively. The variable x indicates the distance to the root of the tooth. Their expressions are given below:

$$\Delta L_x = \begin{cases} 2\sqrt{r^2-(u-x)^2}, & x\in[u-r,u+r] \\ 0, & others \end{cases} \tag{10}$$

$$\Delta A_x = \begin{cases} \Delta L_x \delta, & x\in[u-r,u+r] \\ 0, & others \end{cases} \tag{11}$$

$$\Delta I_x = \begin{cases} \dfrac{1}{12}\Delta L_x \delta^3 + \dfrac{\left(A_x \Delta A_x\left(h_x - \dfrac{\delta}{2}\right)\right)^2}{A_x - \Delta A_x} & x\in[u-r,u+r] \\ 0 & others \end{cases} \tag{12}$$

The geometry of the circular pitting fault is defined by three parameters (see Figure 2): (u) distance between the tooth root and the center of the pit circle, (r) radius of the pit circle, and (δ) pit depth.

For a gear displaying this type of fault, the different components of the mesh stiffness, namely the Hertzian contact stiffness (k_h), the bending stiffness (k_b), the axial stiffness (k_a), and the shear stiffness (k_s), are determined according to the following expressions:

$$k_h = \frac{\pi E\left(L-\Delta L_x\right)}{4\left(1-\mu\right)} \tag{13}$$

 doi:10.20944/preprints202605.0061.v1

$$\frac{1}{k_{b(pitting)}}=\frac{\left[1-\frac{(Z-2.5)(\cos\alpha_1\cos\alpha_2)}{Z\cos\alpha_0}\right]^3-(1-\cos\alpha_1\cos\alpha)^3}{2EL\cos\alpha_1+\sin^3\alpha}+\int_{-\alpha_1}^{\alpha_2}\frac{3\left[1+\cos\alpha_1\left(-\cos\alpha+(\alpha_2-\alpha)\sin\alpha\right)\right]^2(\alpha_2-\alpha)\cos\alpha}{E\left[2L\left((\alpha_2-\alpha)\cos\alpha+\sin\alpha\right)^3-3\frac{\Delta L_x}{R_b}\right]}d\alpha \tag{14}$$

$$\frac{1}{k_{s_{(Pitting)}}}=\frac{1.2(1+v)\cos^2\alpha_1\left(\cos\alpha_2-\frac{Z-2.5}{Z\cos\alpha_0}\cos\alpha_3\right)}{EL\sin\alpha_2}+\int_{-\alpha_1}^{\alpha_2}\frac{1.2(1+v)\cos^2\alpha_1(\alpha_2+\alpha)\cos\alpha\cos^2\alpha_1}{E\left[L\left((\alpha_2-\alpha)cos\alpha+sin\alpha\right)-\frac{1}{2}\frac{\Delta A_x}{R_b}\right]}d\alpha \tag{15}$$

$$\frac{1}{k_{a_{(Pitting)}}}=\frac{\sin^2\alpha_1\left(\cos\alpha_2-\frac{Z-2.5}{Z\cos\alpha_0}\cos\alpha_3\right)}{2EL\sin\alpha_2}+\int_{-\alpha_1}^{\alpha_2}\frac{(\alpha_2+\alpha)\cos\alpha\sin^2\alpha_1}{E\left[2L\left((\alpha_2-\alpha)cos\alpha+sin\alpha\right)-\frac{\Delta A_x}{R_b}\right]}da \tag{16}$$

The effective total mesh stiffness of a pair of spur gears results from the series combination of four components: the bending stiffness k_b, the axial stiffness k_a, the shear stiffness k_s, and the Hertzian contact stiffness k_h. It is expressed as follows:

$$k_{t_{pitted}}=\frac{1}{\frac{1}{k_{h(pit)}}+\frac{1}{K_{b_l(pit)}}+\frac{1}{K_{s_1(pit)}}+\frac{1}{k_{a_1(pit)}}+\frac{1}{k_{b_2(pit)}}+\frac{1}{k_{s_2(pit)}}+\frac{1}{k_{a_2(pit)}}} \tag{17}$$

Circular pitting is characterised by three geometric parameters: the pit depth (δ), the distance between the center of the pit circle and the tooth root (u), and the radius of the pit circle (r).

The total effective mesh stiffness of the spur gear system is the sequential sum of four main contributions: the Hertzian contact stiffness (k_h), the bending stiffness (k_b), the shear stiffness(k_s), and the axial compressive stiffness(k_a).

This calculation applies specifically to the gear (pinion and wheel) affected by the fault.

$$k_t=\left[\frac{1}{\frac{1}{k_{h(pit)}}+\underbrace{\frac{1}{k_{b_l}}+\frac{1}{k_{s_1}}+\frac{1}{k_{a_1}}}_{tooth\ of\ pinion}+\underbrace{\frac{1}{k_{b_2(pit)}}+\frac{1}{k_{s_2(pit)}}+\frac{1}{k_{a_2(pit)}}}_{affected\ tooth\ of\ gear}}\right] \tag{18}$$

After establishing the matrix form of the equations of motion governing the gear system, this section describes their numerical implementation, the simulation parameters selected, as well as a detailed analysis of the dynamic response obtained in a healthy configuration and in the presence of pitting.

Table 1. Basic geometric parameters of spur gears.

Parameters	Values	
	Driving Gear (Pinion)	Driven Gear (Wheel)
Young Module (E) [Pa]	2.068×10^{11}	2.068×10^{11}
Pressure angle (º)	20	20
Poisson's ratio	0.3	0.3

 doi:10.20944/preprints202605.0061.v1

Number of teeth Z_1(pinion) and Z_2 (gear)	30	90
Base circle radius of a pinion R_1 [mm] and gear R_2 [mm]	30.1	76.1
Mass m_1 (pinion) and m_2 (gear) [kg]	0.96	2.88
Meshing stiffness of bearings k_1(pinion) = k_2 (gear) [N.s/m]	6.56×10^7	6.56×10^7
Damping coefficient of bearings C_1(pinion) = C_2 (gear) [N.s/m]	1.8×10^5	1.8×10^5
Torsional stiffness of the coupling k_p (pinion) = k_g (gear) [N.s/m]	4.4×10^4	4.4×10^4
Damping coefficient of the coupling C_p (pinion) = C_g (gear) [N.m. s/rad]	5×10^5	5×10^5

The resulting set of coupled differential equations forms the basis for the numerical simulations and vibration analyses presented in the following sections. These coupled equations were solved numerically using the Runge-Kutta method (MATLAB ode45 integrator). Each simulation was run for 10 s, ensuring a stable dynamic response.

4. Results of Numerical Simulations

To evaluate the dynamic behavior of the proposed gearbox model and to quantify the influence of gear tooth faults, a series of numerical simulations were performed under controlled operating conditions. The simulation results are presented progressively. The analysis starts with a comparison of the stiffness of dynamic gear teeth, followed by a detailed evaluation of the vibration response in the time, frequency, and time frequency domains.

4.1. Numerical Comparison of Dynamic Mesh Stiffness

The equations presented earlier are applied to compare the mesh stiffness of a pair of spur gears running at a speed of 100 rpm, depending on the type of fault and the severity of the pitting. The evolution of this stiffness is illustrated in Figure 3.

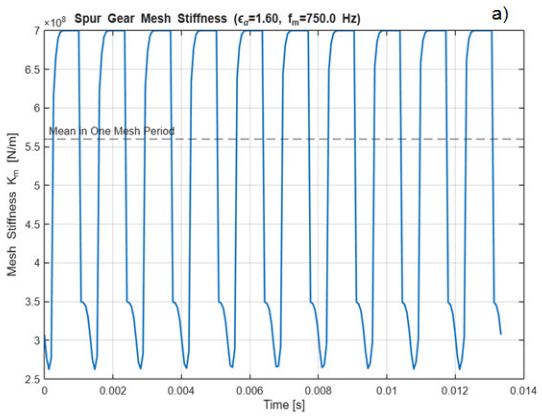

(**a**)

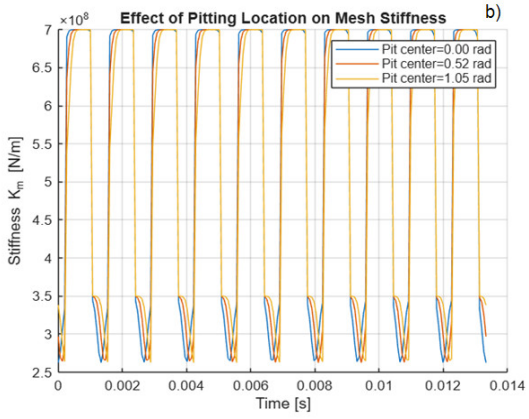

(**b**)

 doi:10.20944/preprints202605.0061.v1

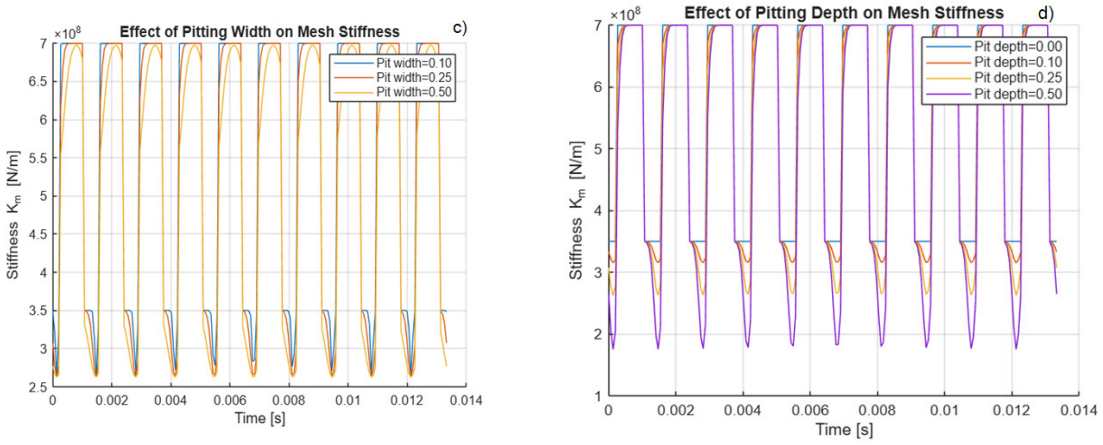

(**c**) (**d**)

Figure 3. Mesh stiffness: healthy (a), and pitted gear (b), (c), (d).

In Figure 3(a), the stiffness curve (blue) shows a smooth and periodic evolution with regular peaks. The maximum stiffness (6.8×10^8 N/m) corresponds to the contact of two pairs of teeth, while the minimum corresponds to contact of a single tooth. This periodic variation is normal and characterizes the effect of the contact ratio in a healthy gear.

In Figure 3(b) under 25% to 50% pitting fault, the gear stiffness undergoes a marked temporal variation, not a simple perturbation. It changes by a factor of 2.5 to 3 over one cycle. This variation directly modulates torsion dynamics and constitutes a primary source of excitation in the drivetrain. Abrupt and periodic changes (non-sinusoidal pulses) generate harmonics of the gear frequency. Significant drops in stiffness during contact transitions increase the relative deflection for a given load, which raises the dynamic transmission error and maximum contact loads (promoting pitting). A higher contact ratio (smoother inlet/outlet) attenuates the amplitude of these decreases and reduces dynamic excitation.

In Figure 3(c) under 25% to 50% pitting fault, it is observed an introduction of a parametric excitation and lateral band modulation in the vibration response caused by the time-varying stiffness asymmetry. The phase shift of the stiffness drops acts as a signature of the pit angular position, useful for the fault localization via synchronous averaging. Each pitting defect produces a specific modulation pattern on the meshing frequency and its harmonics, detectable by vibration analysis.

In Figure 3(d) under 25% to 50% pitting fault, it is observed an increasing of the pitting depth from 0.10 to 0.50 leads to a decrease in the total stiffness amplitude. The stiffness waveform is distorted and becomes asymmetric, indicating a localised loss of stiffness during contact.

The impact patterns shown illustrate how pitting faults affect mesh stiffness. The identification of this influence at different beating percentages, for a speed of 100 rpm, is calculated and presented in Tables 2 and 3.

Table 2. Dynamic effect of pitting on Mesh stiffness.

Pit Center (rad)	Pitting Location on Tooth	Timing of Stiffness Drop	Description of Mesh Stiffness Behavior	Dynamic Effect
0.00 rad	Near tooth root	Early in the meshing cycle	Stiffness decreases at engagement; contact weakens at tooth entry before recovering.	Causes early load fluctuation; increases bending stress at root and risk of crack initiation.
0.52 rad	Around pitch point	Middle of the meshing cycle	Stiffness remains high initially but drops sharply mid-cycle at maximum load transfer.	Most severe effect; amplifies dynamic loads, vibration, and

 doi:10.20944/preprints202605.0061.v1

				noise; reduces load-carrying capacity.
1.05 rad	Near tooth tip	Entire meshing cycle	Stiffness remains stable at engagement and mid-cycle, then decreases near disengagement.	Produces end cycle impact; may induce shock at tooth exit and increase surface wear.

Table 3. Effect of pitting depth and width on mesh stiffness.

Pitting Depth/Width	Mesh Stiffness Behavior	Dynamic Impact
0.00 (Healthy)	Regular periodic pattern, high stiffness	Stable gear meshing
0.10	Slight stiffness reduction	Mild increase in dynamic load
0.25	Noticeable drop and waveform distortion	Increased vibration, sidebands appear
0.50	Large stiffness loss, deep dips	Severe dynamic instability and noise

4.2. Comparing the Dynamic Force Numerically to Predict One-Stage Gearbox System Damage

Time-domain and FFT representations of the simulated vibration responses for the pitting fault condition and the ideal operating condition at speed of 100 rpm, are shown in Figures 4 and 5 respectively.

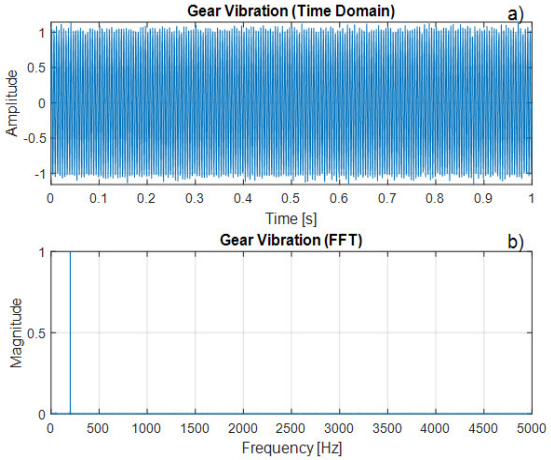

Figure 4. Healthy gear response: (a) Time-domain and (b) FFT at 100 rpm.

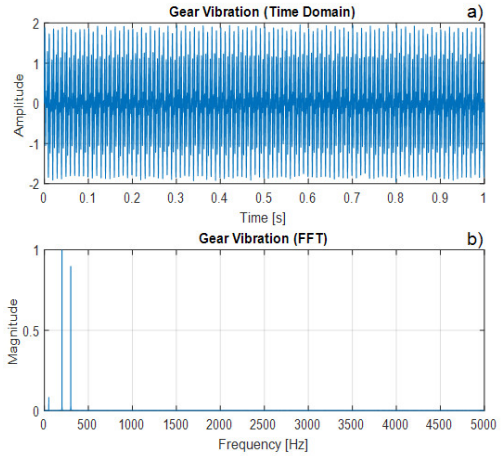

Figure 5. Gear vibration response at 100 rpm: (a) Time-domain and (b) FFT under 25% pitting fault.

 doi:10.20944/preprints202605.0061.v1

In Figure 4 (a), the signal indicates a high-frequency oscillatory vibration with an amplitude ranging from approximately -1 to +1 Hz. The waveform is quasi-periodic, with superimposed slight modulations, which is characteristic of mesh vibrations. The signal is continuous over the one-second window, indicating a steady state vibration response with no apparent transient effects. The primary excitation corresponds to the tooth passage frequency. However, Figure (b), the FFT reveals a sharp spectral peak in the low frequencies (< 500 Hz), with very low energy over this range. A single harmonic is dominant; the rest of the spectrum is virtually flat. This indicates that the vibration is mainly generated by a single source of periodic excitation, probably the mesh or shaft rotational frequency. The absence of broadband components suggests the absence of significant defects, confirming a healthy or near-ideal operating condition.

In Figure 5(a) under 25% pitting fault, the amplitude of the vibration signal (–2 to +2) is slightly larger than that of the healthy state. A high frequency oscillation pattern is observed, accompanied by amplitude modulation, the oscillations are not uniform and their intensity varies periodically. This modulation is usually associated with localised nonlinearities and faults (such as pitting), which disrupt the regular vibration of the mesh. Figure 5(b): The FFT reveals several distinct peaks in the low frequencies (< 500 Hz). Unlike the healthy case (one dominant peak), several frequency components are observed: the mesh frequency, harmonics, and sidebands, which may result from signal modulation induced by the fault. The energy distribution between multiple frequencies indicates that the vibration is not purely sinusoidal and incorporates complex components related to surface damage.

In Figure 6(a) under 50% pitting fault, the signal (–2 to +2) indicates more structured high-frequency oscillations than in the undamaged case, with clear amplitude modulation (periodic variation in intensity). This modulation reveals the influence of additional excitations, likely due to disturbances caused by the fault, on the periodic mesh vibration. However, in Figure 6(d): The spectrum shows several sharp peaks in the low and middle frequencies (< 1000 Hz), with a fundamental component (mesh frequency) and multiple harmonics or sidebands. Compared to the undamaged case, this multiplicity of frequency contributions confirms that the signal is not purely sinusoidal. These additional harmonics are typical of nonlinearities introduced by faults such as tooth pits.

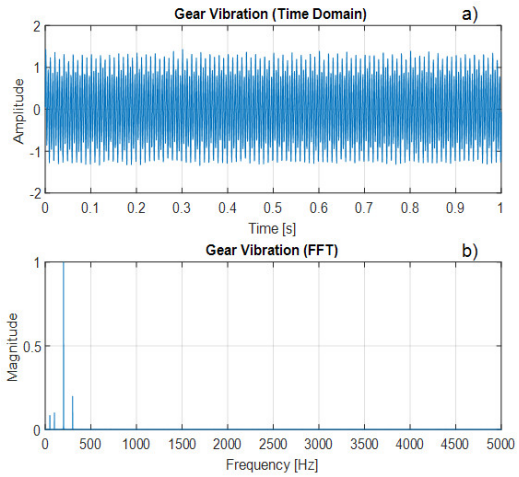

Figure 6. Gear vibration response at 100 rpm:(a) Time-domainand (b) FFT under 50% pitting fault.

4.3. Extraction and Analysis of Pitting Fault Features

To extract the characteristics of pitting faults often masked by torque frequency and the driving forces of the spur gear system a particularly effective method was employed. This method offers a high sensitivity to faults and good diagnostic capabilities.

Quantitative sensitivity analysis was thus able to highlight the nonstationary signatures related to stiffness modulation. It was also revealed that the dominant parameter is the mesh contact ratio at

 doi:10.20944/preprints202605.0061.v1

low velocities and in the early stages of the fault, while pit depth and width become predominant at higher velocities and for advanced pits.

In Figure 7(a), it is observed that the sensitivity of contact ratio ε increases steadily with the gear speed, from 500 to 3000 rpm. The bore related parameters (depth, width, and bore center) remain virtually flat and negligible throughout the velocity range. However, in Figure 7(b), at low and moderate speeds, the system is mainly governed by the mesh geometry and the contact ratio. No frequency component related to a fault (bandwidth, harmonic, and localised peak) is visible. The intersection of the reference curves, representing an increase of 20% and a decrease of 20%, confirms the stability of the gear dynamics in the face of small variations.

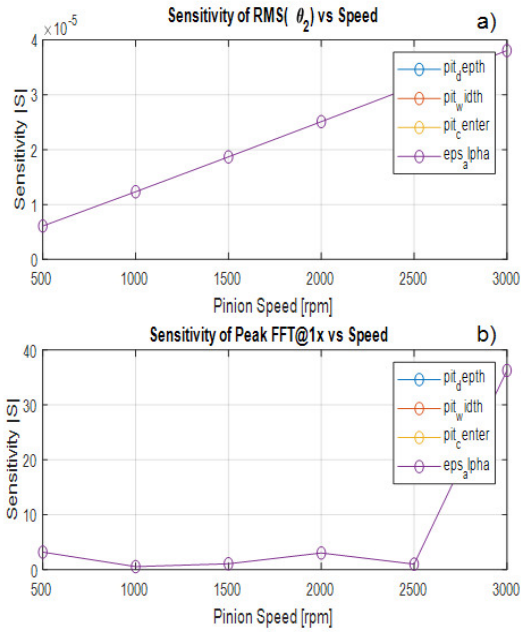

Figure 7. Pinion speed sensitivity of healthy gear: (a) and (b).

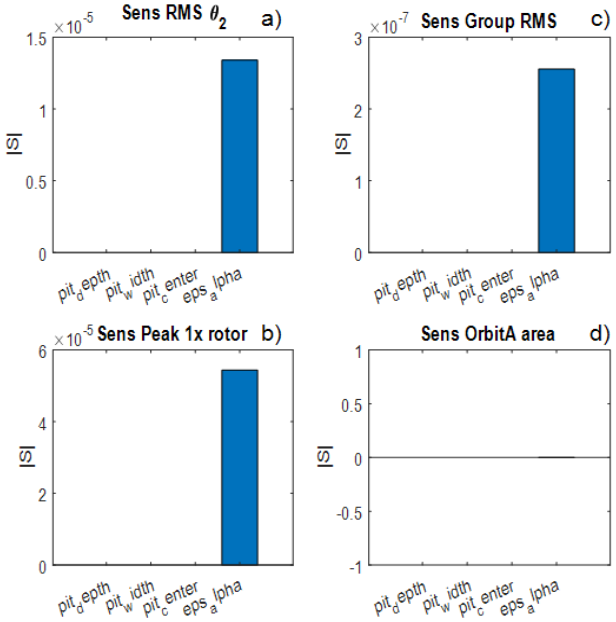

Figure 8. Sensitive magnitude plots for a healthy gear:(a),(b),(c),&(d).

 doi:10.20944/preprints202605.0061.v1

Figure 8 presents four plots where the maximum amplitude |S| is consistently concentrated on the ε_α parameter. This result confirms the behavior of a healthy and fault free gear system. In Figure 8(a), it is observed that the system behaves like an ideal gear pair, the vibration response is not significantly affected by geometric errors but mainly by the tooth contact stiffness. The lack of sensitivity to other parameters is a characteristic signature of a spur gear system in good condition. The analysis continues with Figure 8(b) and Figure 8(c), where the resulting spectrum is very clean and smooth, with a gradual increase in amplitude as a function of frequency. No discrete frequency components related to a defect (bandwidth, harmonic, and localized peak) are visible. The absence of unexpected resonances indicates that the gear system is properly aligned and operating under normal conditions. In contract, in Figure 8(d), all sensitivities are practically zero.

In Figure 9(a) under 25% pitting fault, all parameters indicate very low sensitivity, with the notable exception of ε_α, whose effect is largely dominant. This indicates that, under these conditions, the contact ratio (profile error) influences the system response much more than the pitch-related parameters. The analysis continues with Figure 9(b) where the sensitivity of ε_α remains predominant, but the pitch width now contributes significantly. This means that, in this case, the dynamic response is significantly affected by both the interlocking geometry and the lateral extent of the defect. However, in Figure 9(c), the contributions become more balanced: the depth, width, and position of the pitch all have a non negligible effect. However, ε_α retains the highest sensitivity. Thus, it is observed that the pitch geometry begins to impact the system response, but the contact error at the interlocation remains the most critical factor. In contract, in Figure 9(d), the sensitivity is practically zero for all parameters.

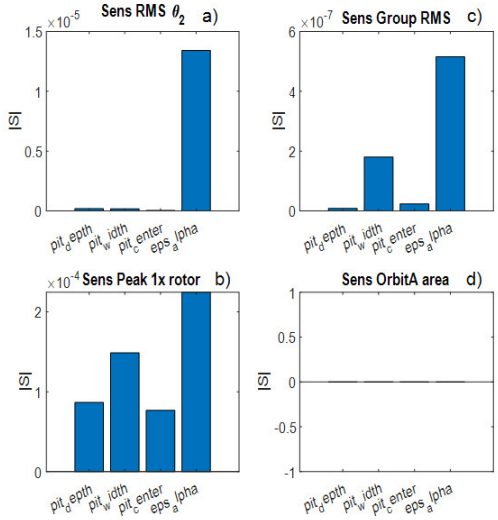

Figure 9. Sensitive magnitude plots for a gear with 25% pitting moderate: (a), (b), (c), and (d).

In Figure 10(a) under 50% pitting fault, the sensitivity is again dominated by ε_α, while the contributions of the pitting depth, width, and position are minimal. In this configuration, geometric accuracy and transmission error govern the system dynamics much more than pitting damage. The analysis continues with Figure 10(b): the pitting length and ε_α indicate a high sensitivity, with the other parameters having a moderate influence. This shows that at this stage, the effects of the fault (through its length) and the mesh error strongly affect the vibrations, indicating an increasing influence of the defect. However, in Figure 10(c), the pitting depth and width become the dominant parameters, submitting ε_α to a secondary role. The failure progress now directly influences the behavior of the system. In contract, in Figure 10(d), all sensitivities are practically zero.

 doi:10.20944/preprints202605.0061.v1

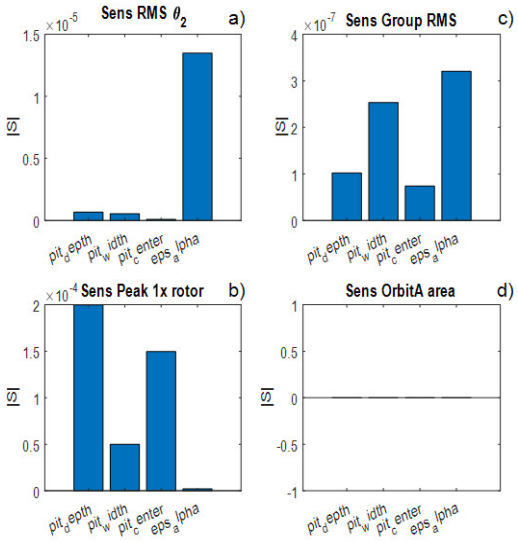

Figure 10. Sensitive magnitude plots for a gear with 50% pitting severity: (a), (b), (c), and (d).

Figure 11(a) indicates that under 25% pitting fault, the sensitivity of the contact ratio (ε_α) increases steadily with pinion speed from 500 to 3000 rpm. The pitting parameters (depth, width, position) remain virtually flat and negligible throughout the speed range. Similarly, at low to moderate speeds as show in Figure 11(b), the dynamics of the system are mainly governed by the mesh geometry and the accuracy of the contact ratio, rather than by surface damage (pitting). The increasing influence of ε_α with speed can be explained by the dynamic amplification of the transmission error at higher frequencies. The very low and constant sensitivity of the pitting parameters indicates that minor defects have minimal impact on the system dynamics within this operating range.

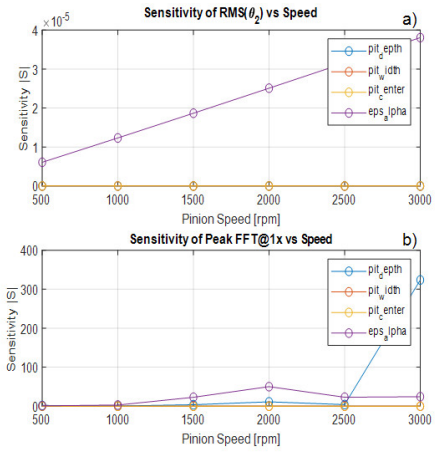

Figure 11. Pinion speed sensitivity analysis under 25% pitting fault: a) Parameter sensitivity trends, b) Vibration spectrum.

Figure 12(a) indicates that under 50% pitting fault, the sensitivity of ε_α (purple line) dominates at all speeds and steadily increases with pinion speed. Pitting sensitivities remain virtually constant and very low. The dynamics of the system are therefore always governed by the contact ratio and the precision of the mesh. The increase in the sensitivity of ε_α with speed corresponds to normal behavior, due to the increase in excitation frequency and charge transfer in the mesh. However, in Figure 12(b) at this advanced stage of pitting, the fault-related sensitivities (particularly depth and width) start to show a significant increase beyond 2000 rpm, while that of ε_α remains influential but fluctuates. The

 doi:10.20944/preprints202605.0061.v1

depth related sensitivity peaks around 2500 rpm, indicating that this parameter begins to significantly affect the system response at high speeds. This increase in sensitivity with speed indicates that the effects of the fault (local stiffness reduction, impacts) are dynamically amplified at high speeds.

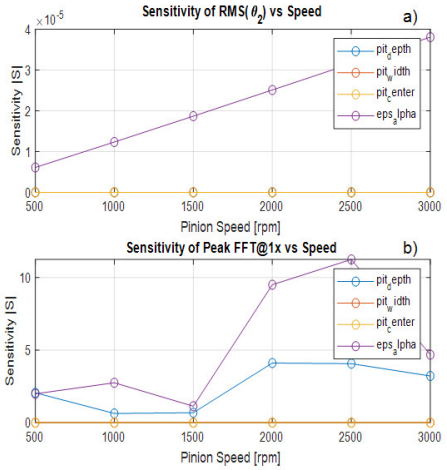

Figure 12. Pinion speed sensitivity analysis under 50% pitting fault: a) Parameter sensitivity trends, b) Vibration spectrum.

5. Discussions

The numerical results clearly demonstrate the significant influence of gear pitting on the variation of mesh stiffness and, consequently, on the dynamic response of the transmission. Under normal conditions, mesh stiffness exhibits a smooth and periodic evolution, corresponding to the single and double-tooth contact phases. This behavior results in stable vibration response, dominated by the fundamental mesh frequency, as shown by the time and frequency domain analyses.

With increasing pitting, the stiffness waveform becomes distorted and asymmetric. Even a moderate level of pitting introduces abrupt decreases in stiffness during meshing. These perturbations act as parametric excitations and generate amplitude modulation in the vibration signal. In FFT spectra, these effects manifest as the appearance of additional harmonics and sidebands around the mesh frequency, consistent with the defect signatures documented in recent numerical and experimental studies.

Sensitivity analysis provides in-depth understanding into the mechanisms of defect propagation. At low pitting levels and low speeds, the vibration response is mainly governed by the contact ratio and transmission error, indicating that the geometric accuracy dominates the system behavior. However, as rotational speed and hole depth increase, the fault related parameters particularly depth and hole width increase significantly in influence. This transition reveals a critical operating regime where localised surface damage is dynamically amplified, significantly affecting system stability.

The results also show that the location of the pit (central position on the tooth) has a relatively weaker influence on the overall vibration indicators. This indicates that severity parameters play a more decisive role than spatial position in the overall dynamic response. These results emphasise the importance of monitoring stiffness related indicators and speed dependent effects to diagnose pitting faults at an early stage.

Overall, the proposed model shows strong physical consistency, with the observed vibration trends closely matching the stiffness degradation mechanisms introduced by pitting progress. The parameter sensitivity based approach provides a solid foundation for prioritising diagnostic features in condition monitoring applications.

 doi:10.20944/preprints202605.0061.v1

6. Conclusions

This study developed a coupled dynamic model with six degrees of freedom (torsion and bending) to analyze the influence of fatigue pitting evolution in a single-stage spur gear reducer. A time-varying mesh stiffness formulation, based on potential energy principles, was proposed to explicitly incorporate pitting geometry specifically, pit depth, radius, and angular position.

The main results can be summarized as follows:

1. The progressive development of pitting leads to stiffness asymmetry and localized reductions, which act as parametric excitations in the system's dynamic equations.
2. Vibration signatures evolve from an essentially harmonic behavior in a healthy regime to spectra marked by amplitude modulation and the appearance of sidebands as damage progresses.
3. Quantitative sensitivity analysis shows that the dominant parameters vary with rotational speed: the gear ratio is crucial at low speeds and in the early stages of failure.

The importance of cavity depth and width becomes evident at high speeds and in advanced stages of degradation.

The severity parameters of defects have a greater impact on dynamic amplification than their spatial location, which highlights their importance for predictive maintenance plans.

The proposed modeling framework provides a mathematically consistent and numerically robust basis for analyzing stiffness modulated gear dynamics. It offers a physically interpretable approach for early fault detection and can contribute to the development of speed adaptive monitoring systems.

Future work will focus on experimental validation, extension to multi-stage gearboxes, and integration with data-driven diagnostic algorithms.

Author Contributions: Y.H.K.H.: conceptualization, methodology, software, validation, formal analysis, data curation, writing—original draft preparation, writing—review and editing. B.X.T.K.: supervision, review and editing. All authors have read and agreed to the published version of the manuscript.

Funding: This research received no external funding.

Data Availability Statement: The data presented in this study are available on request from the corresponding author.

Acknowledgments: The authors are grateful for the resources and equipment provided by the Department of Industrial Engineering, Operation Management, and Mechanical Engineering at Vaal University of Technology (South Africa) to enable this work.

Conflicts of Interest: The authors declare no conflict of interest.

Abbreviations

The following abbreviations are used in this manuscript:

m_1	Pinion mass at the first stage
m_2	Wheel (gear) mass at the first stage
x_1	The linear displacement of the pinion
x_2	The linear displacement of the wheel
y_1	The linear displacement of the pinion
y_2	The linear displacement of the wheel
J_1	Mass moment of inertia of the pinion
J_2	Mass moment of inertia of the wheel

 doi:10.20944/preprints202605.0061.v1

J_m	Mass moment of inertia of the motor
J_L	Mass moment of inertia of the load
k_{y_1}	Stiffness of the input bearing in the **y**-direction
k_{y_2}	Stiffness of the output bearing in the **y**-direction
k_p	Torsional stiffness of the input shaft coupling
k_g	Torsional stiffness of the output shaft coupling
c_g	Torsional damping of the output shaft coupling
c_p	Torsional damping of the input shaft coupling
k_t	Gear meshing stiffness
c_t	Gear meshing damping
θ_1 *and* θ_2	The angular displacement of the pinion and wheel
R_1 *and* R_2	Base circle radius of pinion and wheel
C_{y_1} *and* C_{y_2}	Damping of the input bearing and output bearing

References

1. Junguo W.; Jie Z.; Zhaoyuan Y.; Xufeng Y.; Rui.; Yongxiang Z.; Nonlinear characteristics of a multi-degree-of-freedom spur gear system with bending-torsional coupling vibration, Mechanical Systems and Signal Processing, Volume 121, 2019, pp. 810-827, ISSN 0888-3270, https://doi.org/10.1016/j.ymssp.2018.12.002.
2. Zhang, H. (2025). Gearbox fault diagnosis using a dual-channel fuzzy convolutional neural network with explainable analysis. Nondestructive Testing and Evaluation, 1–25. https://doi.org/10.1080/10589759.2025.2566773.
3. Zeng, Y.; Zhu, J.; Han, Y.; Qiu, D.; Huang, W.; Xu, M. Dynamic Modeling and Numerical Analysis of Gear Transmission System with Localized Defects. Machines 2025, 13, 272. https://doi.org/10.3390/machines 13040272.
4. He, Z., Wang, X., Li, Y. and Yang, Y., 2025. Analysis of Gear System Dynamics Based on Thermal Elastohydrodynamic Lubrication Effects. Lubricants, 13(9), p.411.
5. Yang L.; Natalie B.; Ming L. Dynamical modeling and experimental validation for tooth pitting and spalling in spur gears, Mechanical Systems and Signal Processing, Volume 119, 2019,Pages 155-181,ISSN 0888-3270,https://doi.org/10.1016/j.ymssp.2018.09.027.
6. Liang, X.H., Liu, Z.L., Pan, J. and Zuo, M.J., 2017. Spur gear tooth pitting propagation assessment using model-based analysis. Chinese Journal of Mechanical Engineering, 30(6), pp.1369-1382.
7. El Badaoui , M., Cahouet , V., Guillet , F., Danie`re, J., and Velex, P. "Modeling and Detection of Localized Tooth Defects in Geared Systems."ASME. J.Mech.Des. September 2001;123(3): 422–430. https://doi.org/10.1115/1.1349420
8. Peng, Z.K.; Chu, F.L. Application of the wavelet transform in machine condition monitoring. Mech. Syst. Signal Process. 2004, 18, 199–221.
9. Fu, D.; Gao, S.; Liu, H. Study on Dynamics of a Two-Stage Gear Transmission System with and without Tooth Breakage. Processes 2021, 9, 2141. https://doi.org/10.3390/pr9122141.